



Defect turbulence in a dense suspension of polar, active swimmersNavdeep Rana *Max Planck Institute for Dynamics and Self-Organization (MPIDS), D-37077 Göttingen, Germany*Rayan Chatterjee *Stanford Medicine, Stanford University, Stanford, California 94305, USA*

Sunghan Ro and Dov Levine

Department of Physics, Technion-Israel Institute of Technology, Haifa 3200003, Israel

Sriram Ramaswamy

*Department of Physics, Indian Institute of Science, Bengaluru 560 012, India*Prasad Perlekar ^{*}*Tata Institute of Fundamental Research, Hyderabad 500046, India*

(Received 9 June 2023; accepted 19 January 2024; published 13 February 2024)

We study the effects of inertia in dense suspensions of polar swimmers. The hydrodynamic velocity field and the polar order parameter field describe the dynamics of the suspension. We show that a dimensionless parameter R (ratio of the swimmer self-advection speed to the active stress invasion speed [[Phys. Rev. X **11**, 031063 \(2021\)](#)]) controls the stability of an ordered swimmer suspension. For R smaller than a threshold R_1 , perturbations grow at a rate proportional to their wave number q . Beyond R_1 we show that the growth rate is $\mathcal{O}(q^2)$ until a second threshold $R = R_2$ is reached. The suspension is stable for $R > R_2$. We perform direct numerical simulations to characterize the steady-state properties and observe defect turbulence for $R < R_2$. An investigation of the spatial organization of defects unravels a hidden transition: for small $R \approx 0$ defects are uniformly distributed and cluster as $R \rightarrow R_1$. Beyond R_1 , clustering saturates and defects are arranged in nearly stringlike structures.

DOI: [10.1103/PhysRevE.109.024603](https://doi.org/10.1103/PhysRevE.109.024603)**I. INTRODUCTION**

The instability of a viscous suspension of motile organisms [1–3] leads to an abundance of ordered and chaotic states [4–11], of which *active turbulence* [12–14] has attracted much attention. The majority of studies have investigated this iconic phenomenon in *nematic* systems, where the local structure and characteristic defects are associated with uniaxial fore-aft symmetric order. References [15,16] investigated polar patterns in active fluids and found traveling waves and chaotic regimes. In a recent work [1] we established the stabilizing role of fluid inertia in the transition to active turbulence in *polar* active suspensions, where the local order is vectorial. We discovered that the steady-state behavior of the suspension changed across two thresholds, R_1 and R_2 , in the dimensionless ratio $R \equiv \rho v_0^2 / \sigma$ of inertia and activity, where ρ is the mass density of the suspension, v_0 is the self-propulsion

speed, and σ the mean active stress. We found defect turbulence for $R < R_1$, a fluctuating but ordered phase-turbulent steady state for $R_1 < R < R_2$, and a quiescent ordered state for $R > R_2$. The analysis of [1] considered only the suspension velocity \mathbf{u} and the polar order parameter \mathbf{p} , while implicitly treating the concentration of active particles as “fast.” This approach is justified if the relaxation rate of the concentration fluctuations does not vanish as the wave number goes to zero, as would happen, for example, if the concentration field becomes nonconserved due to the birth and death processes. The relevance of competing influence of inertia and viscous effects for active swimmers was also emphasized in [17], and other recent works have investigated defect dynamics and turbulence in Malthusian polar suspensions with $R = 0$, i.e., without inertial effects [18–21].

Highly concentrated systems [6,22–24] present another scenario where we can ignore fluctuations in the number density of suspended particles, albeit in a radically different manner. In such a limit it is reasonable to make the approximation that the fluctuations in the concentration are negligible compared to its mean value, which means that the solute velocity field or, equivalently, the polar order parameter \mathbf{p} , is solenoidal: $\nabla \cdot \mathbf{p} = 0$. We will term such systems as simply “dense.” See Ref. [24] for the implementation of such a condition in dry active matter.

^{*}perlekar@tifrh.res.in

Published by the American Physical Society under the terms of the [Creative Commons Attribution 4.0 International](#) license. Further distribution of this work must maintain attribution to the author(s) and the published article’s title, journal citation, and DOI. Open access publication funded by the Max Planck Society.

In this paper we study the stability and turbulence in a dense suspension of polar active particles. Section II describes the equations of motion, and in Sec. III we conduct a linear stability analysis of an ordered suspension with respect to perturbations with wave number q . Dense suspensions of contractile swimmers ($\sigma < 0$) are linearly stable. On the other hand, for extensile suspensions ($\sigma > 0$), the same dimensionless parameter R as in [1] governs the linear stability of the suspension. For $R < R_1 \equiv 1 + \lambda$, where λ is the flow-alignment parameter, we find an inviscid instability where the most unstable pure-bend modes grow at a rate $\propto q$. For $R_1 < R < R_2$, we find that the pure-bend perturbations grow at a rate $\propto q^2$. Finally, for $R > R_2$ orientational order is linearly stable. These instability mechanisms are identical to those reported in our earlier work [1]. Next, in Sec. IV we study the steady-state properties of extensile suspension using numerical simulations. We show the presence of vortex-defect turbulence for $R < R_2$. Correlation length grows as we increase R and appears to diverge at $R \approx R_2$. Interestingly, we do not find a phase-turbulent regime [1]. Instead, a detailed analysis of the spatial distribution of defects using the correlation dimension d_2 reveals a novel morphological transition. We find that the defects are uniformly distributed ($d_2 \approx 2$) for $R \rightarrow 0$ (Stokesian suspension) and start to cluster on increasing R . Maximum clustering ($d_2 \approx 1$) is attained at around $R = R_1$, and we observe that defects organize into stringy patterns. No further changes in defect organization are observed on increasing R beyond R_1 .

II. EQUATIONS OF MOTION

We use a hydrodynamic formulation to study the dense suspension of polar active particles. In the dense limit (uniform suspension density and active particle concentration), the dynamics of the hydrodynamic velocity field $\mathbf{u}(\mathbf{x}, t)$ and the orientation order parameter $\mathbf{p}(\mathbf{x}, t)$ is described by the following equations [1,2,4,25–27]:

$$\begin{aligned} \rho(\partial_t \mathbf{u} + \mathbf{u} \cdot \nabla \mathbf{u}) &= -\nabla P + \mu \nabla^2 \mathbf{u} + \nabla \cdot (\boldsymbol{\Sigma}^a + \boldsymbol{\Sigma}^r), \\ \partial_t \mathbf{p} + (\mathbf{u} + v_0 \mathbf{p}) \cdot \nabla \mathbf{p} &= -\nabla \Pi + (\lambda \mathbf{S} + \boldsymbol{\Omega}) \cdot \mathbf{p} + \Gamma \mathbf{h}, \\ \nabla \cdot \mathbf{u} &= 0, \text{ and } \nabla \cdot \mathbf{p} = 0. \end{aligned} \quad (1)$$

Here, ρ is the suspension density, μ is the fluid viscosity, v_0 is the self-advection speed of the swimmers, λ is the flow-alignment parameter, P is the hydrodynamic pressure that enforces incompressibility of the velocity field, Π is the pressurelike term that enforces the solenoidal condition on the order parameter field \mathbf{p} imposed by the constant concentration approximation, and $\mathbf{S} \equiv (\nabla \mathbf{u} + \nabla \mathbf{u}^T)/2$ and $\boldsymbol{\Omega} \equiv (\nabla \mathbf{u} - \nabla \mathbf{u}^T)/2$ are the symmetric and antisymmetric parts of the velocity gradient tensor $\nabla \mathbf{u}$. $\boldsymbol{\Sigma}^a \equiv -\sigma_0 \mathbf{p} \mathbf{p}$ is the leading-order apolar intrinsic stress associated with the swimming activity where the force-dipole density $\sigma_0 > 0 (< 0)$ for extensile (contractile) swimmers [2], $\boldsymbol{\Sigma}^r \equiv -\lambda_+ \mathbf{h} \mathbf{p} - \lambda_- \mathbf{p} \mathbf{h}$ is the reversible thermodynamic stress [27] with $\lambda_{\pm} = (\lambda \pm 1)/2$, $\mathbf{h} = -\delta F / \delta \mathbf{p}$ is the molecular field conjugate to \mathbf{p} with the free-energy functional

$$F = \int d^d r \left[\frac{K}{2} |\nabla \mathbf{p}|^2 + \frac{1}{4} (\mathbf{p} \cdot \mathbf{p} - 1)^2 \right],$$

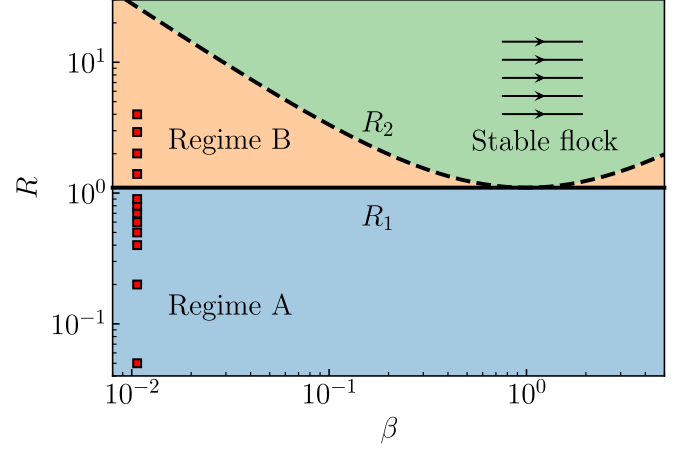


FIG. 1. $R - \beta$ phase diagram highlighting different stability regimes for dense polar active suspensions. In both the unstable regimes A and B, we observe defect turbulence (see Sec. IV). Red squares mark the simulations on the $R - \beta$ plane with $\beta = 10^{-2}$, $R_1 = 1.1$, and $R_2 = 28$. See Table I for the rest of the parameters.

that favors an aligned order parameter state with unit magnitude, and Γ is the rotational mobility for the relaxation of the order parameter field to the uniform ordered state prescribed by the free-energy dynamics. For simplicity we choose a single Frank constant K , which penalizes the gradients in \mathbf{p} [28]. We are primarily interested in the interplay of the self-propulsion speed v_0 and the leading-order apolar active stress, hence similar to our earlier study [1], and have ignored the contribution from higher-order polar gradient terms in $\boldsymbol{\Sigma}^a$.

III. LINEAR STABILITY ANALYSIS

We analyze the stability of the ordered state $(\mathbf{u}, \mathbf{p}) = (0, \hat{x})$ to small monochromatic perturbations of the form $(\delta \mathbf{u}, \delta \mathbf{p}) = (\hat{\mathbf{u}}, \hat{\mathbf{p}}) e^{i(\mathbf{q} \cdot \mathbf{x} - \omega t)}$, where \mathbf{q} is the perturbation wave vector and ω is the frequency. As dense contractile suspensions are linearly stable due to the solenoidal constraint on the order parameter field, here we focus our study on extensile suspension. In what follows we discuss the results for pure-bend perturbations, the most unstable modes for extensile systems [1,5]. In a general description of polar suspensions, the concentration fluctuations only couple to the splay-bend modes; thus the dispersion relations for twist-bend modes are identical for suspensions with “fast” [1], slow, or no concentration fluctuations. For a detailed discussion of the linear stability analysis including the stability of twist-bend and splay-bend modes, we refer the reader to Appendix. A large wavelength (small q) expansion up to $\mathcal{O}(q^2)$ yields the following dispersion relation for the pure-bend modes:

$$\begin{aligned} 2\omega_{\pm} &= v_0(1 \pm \sqrt{1 - R_1/R})q \\ &+ i \frac{\mu}{\rho} \left(\pm \frac{(1 - \beta)}{\sqrt{1 - R_1/R}} - (1 + \beta) \right) q^2, \end{aligned} \quad (2)$$

where we have defined the dimensionless numbers $R \equiv \rho v_0^2 / 2\sigma_0$, $R_1 \equiv 1 + \lambda$, and $\beta = \Gamma K \rho / \mu$. In Fig. 1 we show a qualitative phase diagram highlighting the three different stability regimes. In regime A, $R < R_1$, and irrespective of

TABLE I. Parameters used in our simulations. $\rho = 1$, $\lambda = 0.1$, $\mu = 0.1$, $K = 10^{-3}$, $v_0 = 3.16 \times 10^{-2}$, and $\Gamma = 1$ are kept fixed for all runs. This sets $\beta = 10^{-2}$, $R_1 = 1.1$, and $R_2 = 28$. We vary R by varying σ_0 . The superscripts \star (\dagger) indicate increments of 0.05 (0.1).

L	N	$R \equiv \rho v_0^2 / 2\sigma_0$
10π	1024	0.05
40π	2048	$0.2 - 0.4^\star$
80π	4096	0.5
160π	4096	$0.01, 0.05, 0.6 - 0.9^\dagger$
160π	4096	1.4, 2, 3, 4

the value of β , pure-bend modes are unstable with a growth rate $\Im(\omega) \propto q$. In regime B, $R_1 < R < R_2$, where $R_2 \equiv R_1(1 + \beta)^2/4\beta$, pure-bend modes grow at a rate $\Im(\omega) \propto q^2$. Finally, in regime C, when $R > R_2$ the ordered state is stable.

IV. DIRECT NUMERICAL SIMULATIONS

We perform direct numerical simulations of (1) on a square domain of area L^2 discretized with N^2 equispaced collocation points. Similar to [1], we use a pseudospectral method for spatial integration of the velocity field and a fourth-order finite difference method for the order parameter. For time marching we use a second-order Adams-Bashforth scheme [29], and the solenoidal condition on the order parameter field

is implemented using an operator-splitting method [30]. We undertake high-resolution numerical studies at various values of R and fixed $\beta = 10^{-2}$ to characterize the turbulent states arising from the instabilities of the ordered state. We initialize our simulations with a perturbed ordered state $\mathbf{u}(\mathbf{x}, 0) = \mathbf{0} + A \sum_{i=1}^{10} \cos(q_i x) \hat{y}$ and $\mathbf{p}(\mathbf{x}, 0) = \hat{x} + B \sum_{i=1}^{10} \cos(q_i x) \hat{y}$, where $q_i = i(2\pi/L)$, and choose $A = B = 10^{-3}$. For $R < R_2$, the perturbations destabilize the flow and a defect turbulence state is achieved. Table I summarizes all our simulation parameters. In what follows we discuss the statistical properties of defect turbulence with varying R .

A. Defect turbulence

In Fig. 2 we show the streamlines of the order parameter field \mathbf{p} in the statistically steady state at different values of R . In both regimes A and B, the order parameter field shows vortices and saddles, with no evidence of global polar order. Note that asters and spirals are ruled out by the solenoidal constraint. To further verify that the turbulent states lack global orientational order, we compute the magnitude of the average polar order parameter $|\langle \mathbf{p} \rangle|$ in the statistically steady state at different values R , where $\langle \dots \rangle$ denotes spatiotemporal averaging. Note that for disordered states, $|\langle \mathbf{p} \rangle| = 0$, whereas $|\langle \mathbf{p} \rangle| = 1$ for a perfectly aligned state. In the inset of Fig. 3(c) we plot $|\langle \mathbf{p} \rangle|$ with increasing R , and, as expected, it is close to zero in both the unstable regimes.

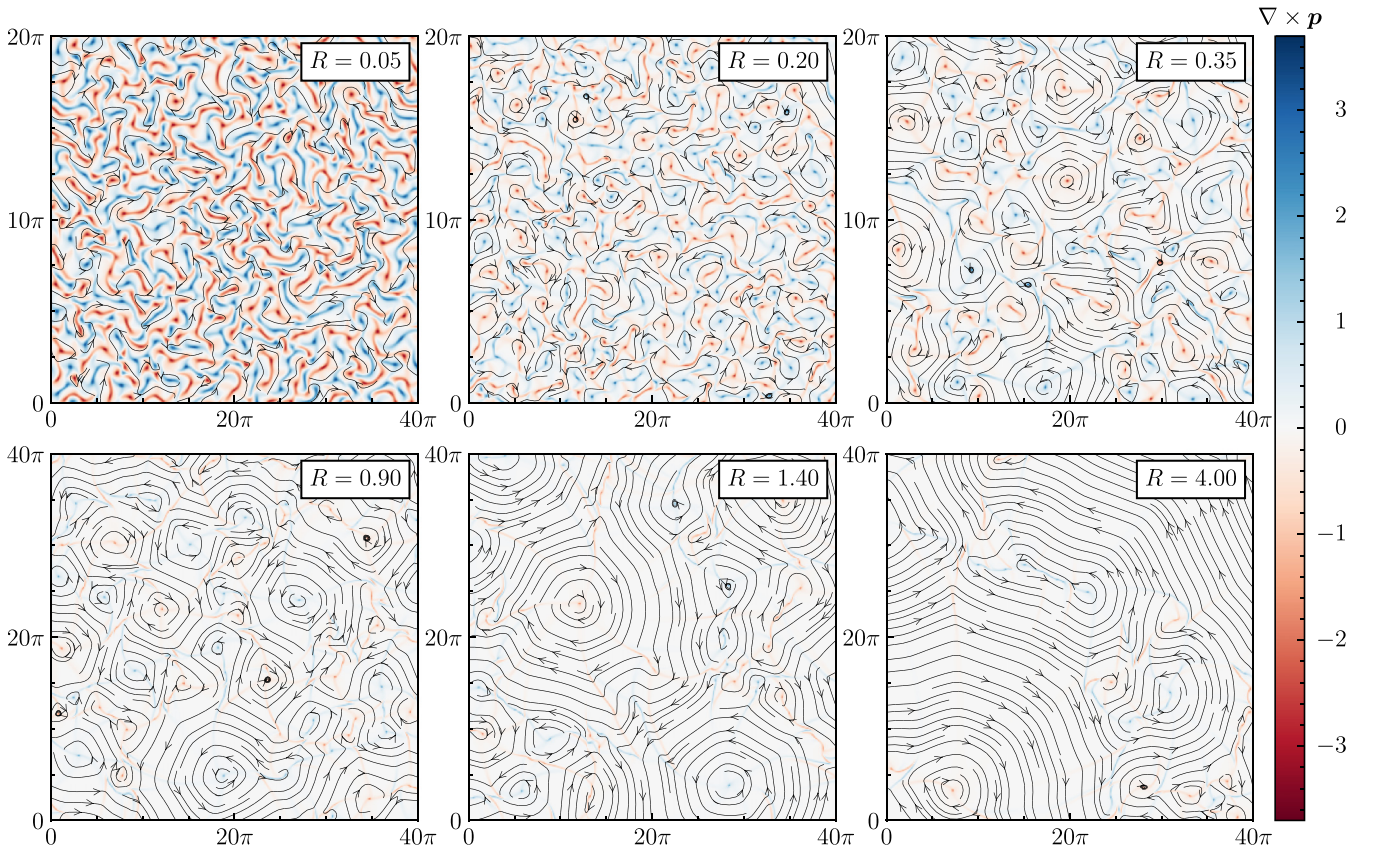


FIG. 2. Order parameter streamlines superimposed over pseudocolor plot of $\nabla \times \mathbf{p}$ highlighting vortices at different values of R . For $R \geq 0.9$ we only show a subdomain of size $(40\pi)^2$. Interdefect separation grows with increasing R . For $R < R_1 = 1.1$, we find that the defects are uniformly distributed over the simulation domain but form clusters for $R > R_1$ (see also Fig. 4).

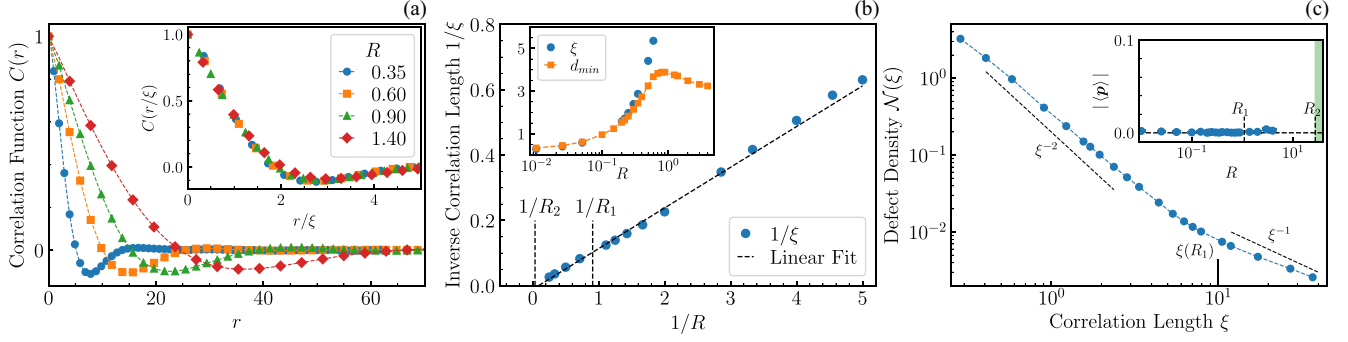


FIG. 3. (a) Steady-state correlation function $C(r)$ for different values of R . (Inset) Correlation function collapse onto a single curve when distance is scaled by the correlation length ξ . (b) Plot of the inverse correlation length $1/\xi$ vs $1/R$. From the intercept of the linear fit on the $1/R$ axis, we conclude that ξ diverges around $R \approx R_2$. Inset: Comparison between the correlation length ξ and average nearest-neighbor distance d_{\min} . For small R , ξ and d_{\min} are identical. For large R , d_{\min} saturates and ξ diverges. (c) Defect density $\mathcal{N}(\xi)$ as a function of the correlation length ξ . We observe two distinct scaling regimes for $R < R_1$ ($> R_1$). Vertical black line marks the correlation length $\xi(R = R_1)$ computed from the linear fit in (B). Inset: We do not observe any significant average order $|\langle p \rangle|$ in the steady state. The ordered state is stable to perturbations in the green shaded region ($R > R_2$).

B. Defect correlations and clustering

In Fig. 3(a) we plot the isotropic correlation function,

$$C(r) = \frac{\langle \mathbf{p}(\mathbf{x} + \mathbf{r}) \cdot \mathbf{p}(\mathbf{x}) \rangle}{\langle \mathbf{p}(\mathbf{x}) \cdot \mathbf{p}(\mathbf{x}) \rangle}, \quad (3)$$

where $\langle \dots \rangle$ denotes ensemble and angle averaging for different values of R . With increasing R , the correlations of the order parameter increase. We fit the functional form $C(r) = e^{-(r/\xi)^\delta}$ at small $r \ll L$ to extract the correlation length ξ and the exponent δ which decreases monotonically from $\delta \approx 1.7$ for $R = 0.2$ to $\delta \rightarrow 1$ for large R . The correlation function $C(r)$ collapses onto a unique curve when plotted versus the scaled separation r/ξ [see Fig. 3(a), inset]. In Fig. 3(b) we show that the correlation length ξ increases with R , and from the intercept of the linear fit on the $1/R$ axis, it appears to diverge at $R = R_2$. Note that investigating the spatial structure of the order parameter field for $R \rightarrow R_2$ becomes numerically unfeasible as $\xi \rightarrow \infty$ and finite-size effects become important.

To quantify the spatial distribution of the defect cores, we begin by identifying the defect coordinates. In the inset of Fig. 3(b) we plot the average nearest-neighbor separation d_{\min} for different values of R . For $R < R_1$, the correlation lengths ξ and d_{\min} are indistinguishable, indicating that a unique length scale describes the defect dynamics [31]. In contrast, for $R > R_1$ correlation length increases, whereas the average nearest-neighbor separation d_{\min} saturates. Consequently, in Fig. 3(c) the defect number density $\mathcal{N}(\xi)$ (number of defects per unit area) also scales differently with the correlation length ξ for $R < R_1$ and $R > R_1$. For $R < R_1$, where a single length scale governs the dynamics, we observe $\mathcal{N}(\xi) \sim \xi^{-2}$, which indicates that the defects are distributed uniformly over the entire domain [32–34]. In contrast, for $R > R_1$ we find that $\mathcal{N}(\xi) \sim \xi^{-1}$, indicating clustering of defects.

Indeed, the scatter plots of the defect coordinates in Figs. 4(a) and 4(b) indicate uniformly distributed defects for $R < R_1$, whereas they appear clustered for $R > R_1$. We further quantify the clustering by evaluating the correlation dimen-

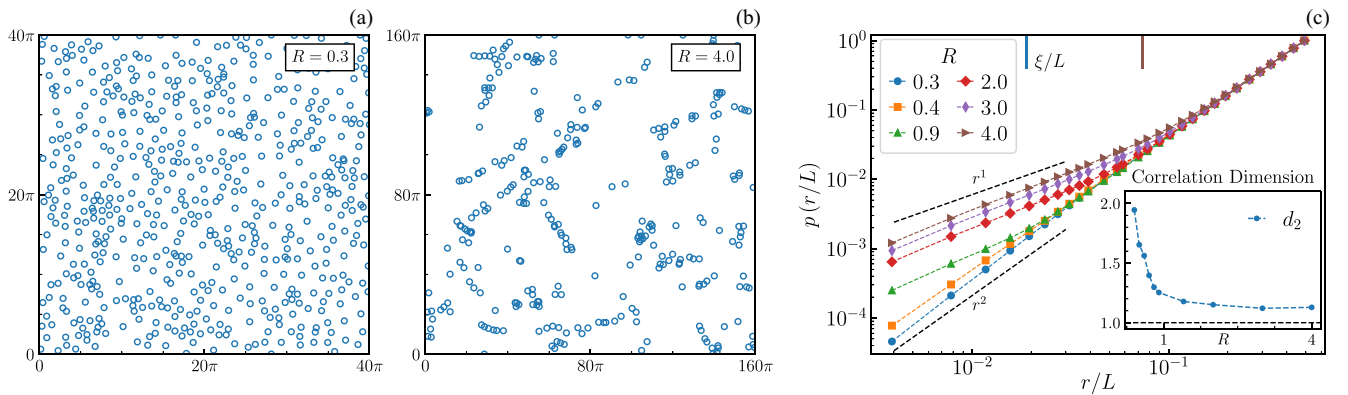


FIG. 4. (a), (b) Scatter plot of the vortex cores for $R = 0.3$ and $R = 4.0$, respectively. For $R = 0.3$ and $R \ll R_1$ in general, defects are uniformly distributed over the simulation domain. For $R \gtrsim R_1$ we observe clustering of defects on one-dimensional stringlike structures. (c) Plot of the cumulative radial distribution function $p(r)$ for different values of R . At smaller distances we observe $p(r) \sim r^{d_2}$, with $d_2 \sim 2$ for $R \ll R_1$ and $d_2 \sim 1$ for $R \gtrsim R_1$ ($p(r) \sim r^1$). At distances larger than typical cluster size, $p(r) \sim r^{-2}$ shows the same scaling for all R . Note that we have rescaled each $p(r)$ curve by its maximum value to highlight different scaling regimes. Inset: Variation of the correlation dimension d_2 vs R obtained from least-squares fit on $p(r)$ for small r .

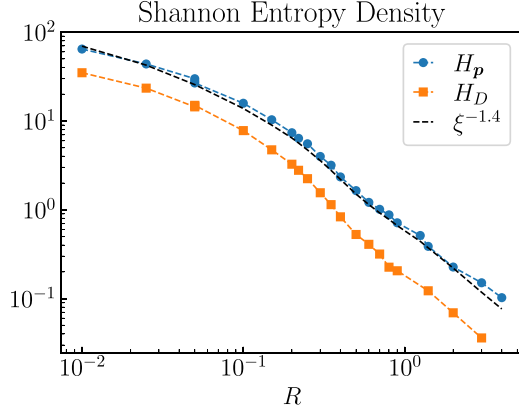


FIG. 5. Plot of the Shannon entropy density H_p of the polar order parameter and the Shannon entropy density of the defect arrangement H_D . With increasing R , both H_p and H_D decrease and scale roughly as $\xi^{-1.4}$ (dashed black guiding line).

sion d_2 from the defect positions. The correlation dimension d_2 is evaluated from the $r \rightarrow 0$ scaling behavior of the probability $p(r)$ of finding two defects within a distance r [35,36]. For $R \ll 1$ we find $d_2 \sim 2$, and it decreases with increasing R until it saturates at around $d_2 \sim 1$ for $R > R_1$ [see Fig. 4(c)]. Thus we conclude that in dense suspensions the crossover in the $O(q)$ to $O(q^2)$ instability around $R = R_1$ is marked by an intriguing defect clustering transition. Qualitatively, the observed defect clustering can be understood by noting that the larger vortex structures are formed in the order parameter field as we increase R . Intense shear regions are created at the boundaries of two such counter-rotating vortices (positive defects), which lead to the formation of multiple vortex-saddle pairs (positive-negative defects) in a stringlike arrangement similar to a Kelvin-Helmholtz instability [37].

In order to gain further insight into the defect clustering transition, we use the Shannon entropy as a proxy for the heat capacity in the equilibrium phase transition and examine any singular signatures. To do so we compute the Shannon entropy density of the polar order parameter H_p and the defect arrangement H_D using a two-dimensional extension of the pattern matching method from information theory [38–40]. To find H_p we apply the pattern matching method on the discretized orientation field [41]. For the entropy density H_D , we apply the pattern matching algorithm on a boolean field that is set to 1 at the defect locations and zero everywhere else (see Fig. 4). In Fig. 5 we plot H_p and H_D versus R . As the defect position field contains less information in comparison to the order parameter field, H_D is smaller than H_p for all R . Both entropy densities decrease as we increase R and scale inversely with the correlation length roughly as $H_D, H_p \approx \xi^{-1.4}$. However, we could not capture a pronounced change in the trend of H_p or H_D that corresponds to the clustering transition at around $R \simeq R_1$. The Shannon entropy does not show a singular feature at $R = R_1$, which suggests that the defect clustering transition may not involve broken symmetries, similar to the case of the Kosterlitz-Thouless transition [42–46].

C. Energy spectrum

The shell-averaged energy spectra for the velocity and the order parameter field are defined as

$$E_u(q) = \sum_{q - \frac{\pi}{L} \leq |m| < q + \frac{\pi}{L}} |\hat{u}_m|^2, \text{ and} \quad (4)$$

$$E_p(q) = \sum_{q - \frac{\pi}{L} \leq |m| < q + \frac{\pi}{L}} |\hat{p}_m|^2,$$

where \hat{u}_m and \hat{p}_m are the Fourier coefficients of the velocity \mathbf{u} and the order parameter \mathbf{p} fields. In Fig. 6 we plot $E_u(q\xi)$ and $E_p(q\xi)$, averaged over the steady-state configurations, for different values of R . Consistent with our correlation function plots, we find that the spectra collapse onto a single curve for $q < q_\sigma$, where $q_\sigma = 2\pi/\ell_\sigma$, and $\ell_\sigma \equiv \mu/\sqrt{\rho\sigma_0}$ is the length scale below which viscosity dominates over active stress. The order parameter spectra show multiple distinct power law scaling regimes,

$$E_p(q\xi) = \begin{cases} q & \text{for } q\xi \rightarrow 0 \\ q^{-(d_2+1)} & \text{for } 1 < q\xi < q_\sigma\xi \end{cases}, \quad (5)$$

which we now describe in detail.

For the smallest $R \leq 0.01$, the correlation length ξ becomes comparable to ℓ_σ , and the order parameter fluctuations become uncorrelated at large scales; thus $E_p(q) \sim q$ as $q \rightarrow 0$ [see Fig. 6(a)] [1]. Consequently, we expect the stress correlations to also become uncorrelated, leading to the Ornstein-Zernike $E_u(q) \sim q/[(q\ell_\tau)^c + 1]$ form of the kinetic energy spectrum [1,47]. For $R = 0.01$, using a least-squares fit, we obtain $\ell_\tau \sim 11\xi$ and $c = 2.5$, close to the expected value $c = 2$. As $R \rightarrow 0$, $\ell_\tau \gg \xi$ and the peak of the spectra will shift to small q , resulting in $E_u(q) \sim q^{-1}$ scaling. This analysis naturally recovers the universal scaling regime of active turbulence [1,18].

On further increasing R , a new scaling range $1 < q\xi < q_\sigma\xi$ appears. For $R = 0.35 (\ll R_1)$, defects are uniformly distributed (see Fig. 4). In this case we observe Porod's scaling in the order parameter spectra scales as $E_p \sim q^{-(d+n)+1}$, where $d = 2$ is the number of dimensions and $n = 2$ is the number of components of the order parameter [34,48]. With increasing R , defects start to cluster and we observe a change in the scaling law. Using d_2 as the effective dimension in Porod's scaling leads to $E_p \sim q^{-(d_2+1)}$. For $R = 0.6$, $d_2 \sim 1.5$ leading to $E_p(q) \sim q^{-2.5}$. Finally, at $R = 2 (> R_1)$, $d_2 \sim 1.1$ saturates, which yields $E_p \sim q^{-2.1}$ [Fig. 6(b)]. For $q\xi > q_\sigma\xi$, dissipative effects dominate, and we observe an exponential decay in the order parameter spectrum.

The kinetic energy spectrum $E_u(q\xi)$ at all R is easily determined by the balance of the viscous and active stresses,

$$\langle\langle |\hat{u}_q|^2 \rangle\rangle \approx -\frac{\sigma_0}{2\mu q^2} \langle\langle \hat{u}_q^* \cdot \hat{f}_q \rangle\rangle, \quad (6)$$

where $\hat{f}_q = \mathcal{P} \cdot (iq \cdot \hat{p} \hat{p}_q)$, \mathcal{P} is the projection operator, and $\langle\langle \cdot \rangle\rangle$ denotes temporal averaging. In Figs. 6(c) and 6(d) we show an excellent agreement between the energy spectrum obtained directly from the velocity field, and using Eq. (6),

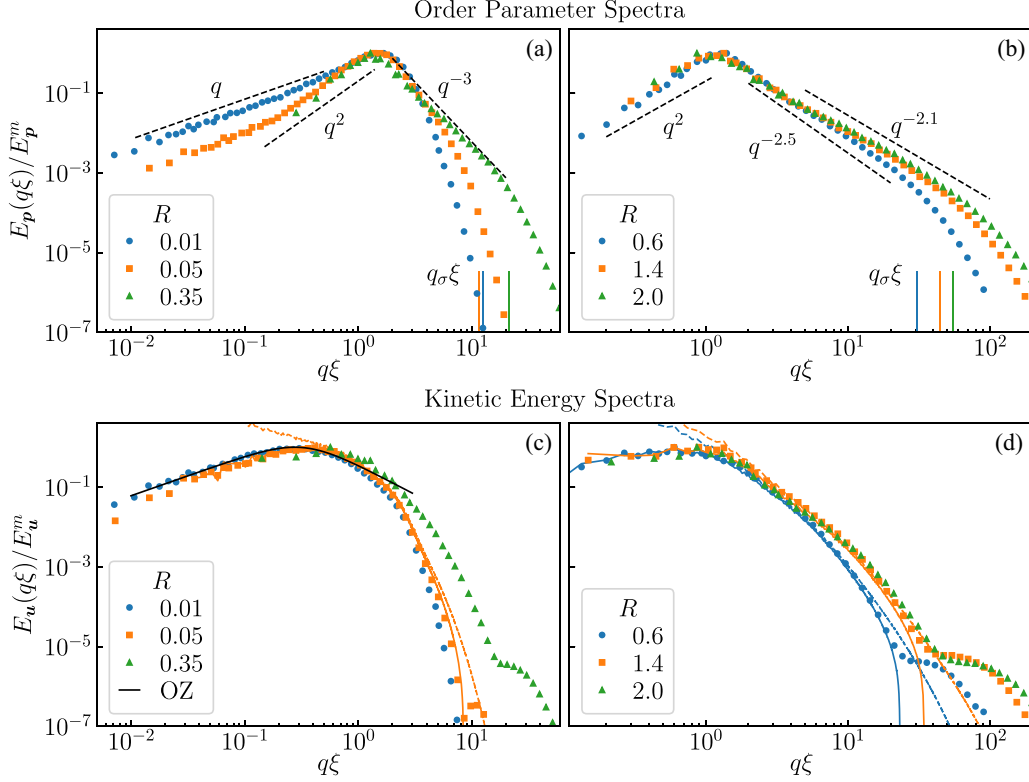


FIG. 6. Plot of the order parameter spectrum $E_p(q\xi)$ and the kinetic energy spectrum $E_u(q\xi)$ for different values of R . We scale the spectra by their respective peak values for data collapse on the y axis. (a) $E_p(q\xi)$ for small R . For $q\xi \ll 1$, $E_p \sim q$. For $q\xi \lesssim 1$, we also observe an intermediate q^2 scaling which vanishes when $R \rightarrow 0$. For small R , defects are uniformly distributed in the simulation domain and thus we observe Porod's scaling between $1 < q\xi < q_\sigma\xi$, best seen for $R = 0.35$. (b) $E_p(q\xi)$ for large R . For $R \lesssim R_1$, d_2 changes continuously and we find a scaling of q^{-d_2-1} . As an example, $d_2 = 1.5$ for $R = 0.6$, thus $E_p \sim q^{-2.5}$. For $R > R_1$ defects cluster and correlation dimension saturates to $d_2 \sim 1.1$, which implies that $E_p \sim q^{-2.1}$, as is evident for $R = 1.4$ and $R = 2.0$. (c, d) $E_u(q\xi)$ for various R . For $R \rightarrow 0$, active stress is spatially uncorrelated. A least-squares fit of the Ornstein-Zernike form $E_u(q) = aq/[(q\ell_\tau)^c + 1]$ for the smallest $R = 0.01$ (solid black line) gives $a = 7.4 \times 10^{-6}$, $\ell_\tau = 3.08 \sim 11\xi$, and $c = 2.5$. For all R , a balance between viscous and active stresses predicts the kinetic energy spectrum very well, as shown in (c, d) for few R by solid and dashed lines of same colors as markers for (6) and (7), respectively.

confirming the dominant balance between viscous and active stresses. Further assuming $\hat{\mathbf{f}}_q$ to be Gaussian random variables and using Gaussian integration by parts [49] we get

$$\langle\langle |\hat{\mathbf{u}}_q|^2 \rangle\rangle = \left\langle\left\langle \frac{\delta \hat{\mathbf{u}}_q}{\delta \hat{\mathbf{f}}_q} \right\rangle\right\rangle \langle\langle \hat{\mathbf{f}}_q^* \cdot \hat{\mathbf{f}}_q \rangle\rangle \approx \frac{\sigma_0^2}{2\mu^2 q^4} \langle\langle \hat{\mathbf{f}}_q^* \cdot \hat{\mathbf{f}}_q \rangle\rangle. \quad (7)$$

We observe that the prediction (7) matches well with the energy spectrum for $1 < q\xi < q_\sigma\xi$.

V. CONCLUSIONS

We study spatiotemporal properties of dense wet suspensions of polar active particles. For such systems, fluctuations in active particle concentration are small compared to its average value and thus we can ignore them. Using a linear stability analysis, we show that inertia can stabilize the orientational order against small perturbations. Our study reveals that the dimensionless parameter $R \equiv \rho v_0^2 / 2\sigma_0$ characterizes the stability of the aligned state. Physically, R is a squared ratio of two speeds: the self-propulsion velocity v_0 and the speed at which active stresses invade through the system $\sqrt{\sigma_0/\rho}$. For $R \gg 1$, the swimmers can outrun the fluctuations induced by active stresses and order persists in the system.

This mechanism is identical to the previously studied case of Malthusian suspensions, where concentration fluctuations are rendered “fast” [1] as a consequence of birth-death processes. However, our numerical studies reveal that these two different limits show distinct steady-state properties. Dense suspensions do not show phase turbulence, and for $R < R_2$ we observe defect turbulence. The order parameter flow consists of topological defects (vortices and saddles) with no global polar or nematic order. We unravel a hidden defect-ordering transition by investigating the spatial organization of defect centers. For $R \rightarrow 0$, defects are uniformly distributed and start to cluster with increasing R . The clustering saturates around $R = R_1$, where we observe that the defects organize onto nearly one-dimensional, stringlike structures. Finally, we show that the spectrum of the order-parameter field shows a Porod's scaling for $q\xi \gg 1$, and a balance of viscous and apolar active stress determines the kinetic energy spectrum of the suspension velocity.

ACKNOWLEDGMENTS

S.R. acknowledges research support from a J. C. Bose Fellowship of the SERB, India. D.L. thanks the Israel Science Foundation for support through Grant No. 2083/23.

P.P. acknowledges support from the Department of Atomic Energy (DAE), India under Project Identification No. RTI 4007, and DST (India) Projects No. MTR/2022/000867, and

No. DST/NSM/R&D HPC Applications/Extension/2023/08. All the simulations are performed using the HPC facility at TIFR Hyderabad.

APPENDIX: LINEAR STABILITY ANALYSIS

We analyze the stability of the ordered state $\mathbf{u} = 0$, $\mathbf{p} = \hat{x}$ to small perturbations $\delta\mathbf{u} \equiv (\delta u_x, \delta\mathbf{u}_\perp)$ and $\delta\mathbf{p} \equiv (\delta p_x, \delta\mathbf{p}_\perp)$, where \perp denotes the plane perpendicular to the ordering. The linearized equations are

$$\begin{aligned}\rho\partial_t\delta u_x &= -\partial_x P + \mu\nabla^2\delta u_x - \partial_x(\sigma_0\delta p_x + \lambda_+K\nabla^2\delta p_x - 2\lambda\delta p_x), \\ \rho\partial_t\delta\mathbf{u}_\perp &= -\nabla_\perp P + \mu\nabla^2\delta\mathbf{u}_\perp - \partial_x(\sigma_0\delta\mathbf{p}_\perp + \lambda_+K\nabla^2\delta\mathbf{p}_\perp), \\ \partial_t\delta p_x &= -\partial_x\Pi - v_0\partial_x\delta p_x + \Gamma K\nabla^2\delta p_x - 2\Gamma\delta p_x + \lambda\partial_x\delta u_x, \\ \partial_t\delta\mathbf{p}_\perp &= -\nabla_\perp\Pi - v_0\partial_x\delta\mathbf{p}_\perp + \Gamma K\nabla^2\delta\mathbf{p}_\perp + \lambda_+\partial_x\delta\mathbf{u}_\perp + \lambda_-\nabla_\perp\delta u_x.\end{aligned}\quad (\text{A1})$$

Note that the perturbations also satisfy the solenoidal criteria, $\nabla \cdot \delta\mathbf{u} = 0$, and $\nabla \cdot \delta\mathbf{p} = 0$. To proceed further, we consider monochromatic perturbations of the form $(\delta\mathbf{u}, \delta\mathbf{p}) = (\hat{\mathbf{u}}, \hat{\mathbf{p}})e^{i(\mathbf{q}\cdot\mathbf{x} - \omega t)}$, where $\mathbf{q} \equiv (q_x\hat{x} + \mathbf{q}_\perp \cdot \perp) = q(\cos\phi\hat{x} + \sin\phi\perp)$ is the perturbation wave vector and $\omega = \Re(\omega) + i\Im(\omega)$. The system is linearly unstable when $\Im(\omega)$. We eliminate the pressure terms and the longitudinal components to obtain

$$\begin{aligned}(-i\rho\omega + \mu q^2)\hat{\mathbf{u}}_\perp &= 2i\lambda q_x \frac{\mathbf{q}_\perp \cdot \hat{\mathbf{p}}_\perp}{q^2} \mathbf{q}_\perp - iq_x(\sigma_0 - \lambda_+Kq^2)\hat{\mathbf{p}}_\perp \\ (-i\omega + \Gamma Kq^2 + iv_0q_x)\hat{\mathbf{p}}_\perp &= -2\Gamma \frac{\mathbf{q}_\perp \cdot \hat{\mathbf{p}}_\perp}{q^2} \mathbf{q}_\perp + i\lambda_+q_x\hat{\mathbf{u}}_\perp.\end{aligned}\quad (\text{A2})$$

The linear system (A2) is a set of four (two) coupled equations in three (two) dimensions and is easily solved by decomposing into splay-bend and twist-bend modes [1,2,45,50]. Taking a dot product with \mathbf{q}_\perp and solving for ω gives the following dispersion relation for the two-dimensional splay-bend modes:

$$\begin{aligned}2\omega_\pm^s &= v_0q\cos\phi - i\frac{\mu_+}{\rho}q^2 - 2i\Gamma\sin^2\phi \\ &\pm \frac{1}{\rho}\sqrt{(\rho v_0q\cos\phi + i\mu_-q^2 - 2i\rho\Gamma\sin^2\phi)^2 - 4\rho\lambda_+q^2\cos^2\phi(\sigma_0 - \lambda_+Kq^2 - 2\lambda\sin^2\phi)},\end{aligned}\quad (\text{A3})$$

where $\mu_\pm = \mu(1 \pm \beta)$. Similarly, a cross product with \mathbf{q}_\perp yields the following solutions for the three-dimensional twist-bend modes:

$$2\omega'_\pm = v_0q\cos\phi - i\frac{\mu_+}{\rho}q^2 \pm \frac{1}{\rho}\sqrt{(\rho v_0q\cos\phi + i\mu_-q^2)^2 - 4\rho\lambda_+q^2\cos^2\phi(\sigma_0 - \lambda_+Kq^2)}.\quad (\text{A4})$$

In two dimensions, ω has two solutions given by Eq. (A3). Additionally, in a general description of polar suspensions, the concentration fluctuations only couple to the splay-bend modes; thus the dispersion relations for twist-bend modes are identical for suspensions with fast [1], slow, or no concentration fluctuations.

1. Extensile suspensions

For extensile systems, the most unstable modes are the pure-bend modes with $\phi = 0$ [1]. In this case, (A3) and (A4) are identical, and as discussed in the main text, a small q expansion reveals that the stability of the pure-bend modes is governed by R . In Figs. 7(a) and 7(b) we plot the growth rate $\Im(\omega)$ vs q for pure bend modes at different values of R in regimes A and B, respectively. The growth rate for a given $q \neq 0$ decreases with increasing R and is an order of magnitude smaller in regime B as compared to regime A.

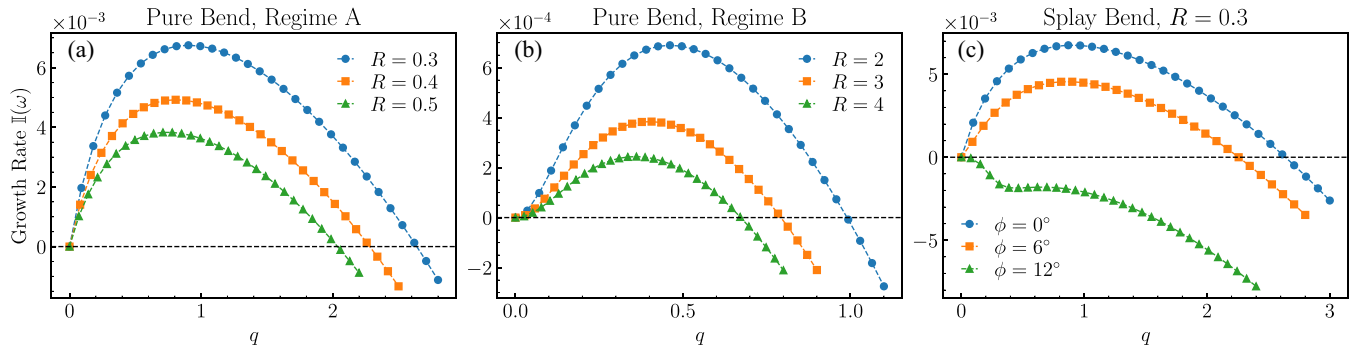


FIG. 7. (a), (b) Growth rate $\Gamma(\omega)$ vs q for the most unstable pure-bend modes at various R in regimes A and B, respectively. With increasing R , the growth rate and the range of unstable wave numbers decreases. (c) Growth rate $\Gamma(\omega)$ vs q for the splay-bend modes at small values of ϕ for a fixed $R = 0.3$.

The solenoidal constraint has major consequences on the stability of the $\phi \neq 0$ modes. The longitudinal and transverse fluctuations are coupled to each other and thus δp_x cannot be rendered *fast*, as was done previously in [1]. Further, the splay deformations are eliminated by an equal and opposite contribution in the transverse direction, which has a q -independent stabilizing effect. The relaxation rate does not vanish in the $q \rightarrow 0$ limit, and at $q = 0$ we have one nonvanishing eigenvalue $\omega^s = -2i\Gamma \sin^2 \phi$, which is a remnant of the coupling between δp_x and δp_\perp . For small but nonzero ϕ , the splay contribution to these modes is small, and they go unstable in a manner similar to the pure bend modes but with a smaller growth rate and a smaller range of unstable wave numbers. In Fig. 7(c) we plot $\Gamma(\omega)$ vs q for various values of ϕ at $R = 0.3$ and verify that indeed it is the case. The stability of the twist-bend modes is identical to that of the pure-bend modes, i.e.,

depending on the various values of R , we obtain three distinct regimes (see Fig. 1 in main text) but with a ϕ -dependent R_1 and R_2 . The dispersion relation for pure twist modes [$\phi = \pi/2$ in (A4)] reduces to $\omega_\pm^t = -\frac{i}{2\rho}(\mu_+ \mp \mu_-)q^2$, implying that the pure twist modes are stable to linear perturbations.

2. Contractile suspensions

Contractile suspensions go unstable via two-dimensional splay perturbations and as a direct consequence of the solenoidal constraint on the order parameter, are always stable. This can also be verified directly from Eqs. (A3) and (A4). For example, the pure splay modes ($\phi = \pi/2$) relax with rates $\omega^s = (-i\frac{\mu}{\rho}q^2, -2i\Gamma)$, and twist-bend modes are always stable as $R < 0$.

- [1] R. Chatterjee, N. Rana, R. A. Simha, P. Perlekar, and S. Ramaswamy, *Phys. Rev. X* **11**, 031063 (2021).
- [2] R. A. Simha and S. Ramaswamy, *Phys. Rev. Lett.* **89**, 058101 (2002).
- [3] S. Ramaswamy, *Nat. Rev. Phys.* **1**, 640 (2019).
- [4] M. C. Marchetti, J. F. Joanny, S. Ramaswamy, T. B. Liverpool, J. Prost, M. Rao, and R. A. Simha, *Rev. Mod. Phys.* **85**, 1143 (2013).
- [5] S. Ramaswamy, *Annu. Rev. Condens. Matter Phys.* **1**, 323 (2010).
- [6] H. H. Wensink, J. Dunkel, S. Heidenreich, K. Drescher, R. E. Goldstein, H. Lowen, and J. M. Yeomans, *Proc. Natl. Acad. Sci.* **109**, 14308 (2012).
- [7] C. Dombrowski, L. Cisneros, S. Chatkaew, R. E. Goldstein, and J. O. Kessler, *Phys. Rev. Lett.* **93**, 098103 (2004).
- [8] L. Giomi, *Phys. Rev. X* **5**, 031003 (2015).
- [9] E. Lauga, *Annu. Rev. Fluid Mech.* **48**, 105 (2016).
- [10] E. Lauga and R. E. Goldstein, *Phys. Today* **65**(9), 30 (2012).
- [11] E. Lauga and T. R. Powers, *Rep. Prog. Phys.* **72**, 096601 (2009).
- [12] R. Alert, J. Casademunt, and J.-F. Joanny, *Annu. Rev. Condens. Matter Phys.* **13**, 143 (2022).
- [13] S. P. Thampi, R. Golestanian, and J. M. Yeomans, *Philos. Trans. R. Soc. Math. Phys. Eng. Sci.* **372**, 20130366 (2014).
- [14] S. Thampi and J. Yeomans, *Eur. Phys. J. Spec. Top.* **225**, 651 (2016).
- [15] L. Giomi and M. C. Marchetti, *Soft Matter* **8**, 129 (2012).
- [16] F. Bonelli, G. Gonnella, A. Tiribocchi, and D. Marenduzzo, *Eur. Phys. J. E* **39**, 1 (2016).
- [17] D. Klotsa, *Soft Matter* **15**, 8946 (2019).
- [18] R. Alert, J.-F. Joanny, and J. Casademunt, *Nat. Phys.* **16**, 682 (2020).
- [19] L. N. Carenza, L. Biferale, and G. Gonnella, *Phys. Rev. Fluids* **5**, 011302(R) (2020).
- [20] A. Amiri, R. Mueller, and A. Doostmohammadi, *J. Phys. A: Math. Theor.* **55**, 094002 (2022).
- [21] B. H. Andersen, J. Renaud, J. Rønning, L. Angheluta, and A. Doostmohammadi, *Phys. Rev. Fluids* **8**, 063101 (2023).
- [22] V. Bratanov, F. Jenko, and E. Frey, *Proc. Natl. Acad. Sci. USA* **112**, 15048 (2015).
- [23] A. Bricard, J.-B. Caussin, N. Desreumaux, O. Dauchot, and D. Bartolo, *Nature (London)* **503**, 95 (2013).
- [24] L. Chen, C. F. Lee, and J. Toner, *Nat. Commun.* **7**, 12215 (2016).
- [25] M. E. Cates and E. Tjhung, *J. Fluid Mech.* **836**, P1 (2018).
- [26] P. Lenz, *Cell Motility* (Springer Science+Business Media, LLC, New York, 2008).

- [27] K. Kruse, J. F. Joanny, F. Jülicher, J. Prost, and K. Sekimoto, *Eur. Phys. J. E* **16**, 5 (2005).
- [28] P. G. de Gennes and J. Prost, *The Physics of Liquid Crystals*, 2nd ed., Oxford Science Publications No. 83 (Oxford University Press, Oxford, England, 1993).
- [29] S. Cox and P. Matthews, *J. Comput. Phys.* **176**, 430 (2002).
- [30] C. Canuto, M. Y. Hussaini, A. Quarteroni, and T. A. Zang, *Spectral Methods in Fluid Dynamics* (Springer, Berlin, Heidelberg, 1988).
- [31] In the limit $R \rightarrow 0$, we expect ξ (or d_{\min}) to saturate to a value proportional to the core-radius of defects $\ell_c \equiv \sqrt{K}$ (independent of R).
- [32] S. Chandrasekhar, *Rev. Mod. Phys.* **15**, 1 (1943).
- [33] P. Hertz, *Math. Ann.* **67**, 387 (1909).
- [34] N. Rana and P. Perlekar, *Phys. Rev. E* **102**, 032617 (2020).
- [35] P. Grassberger and I. Procaccia, *Physica D* **9**, 189 (1983).
- [36] D. Mitra and P. Perlekar, *Phys. Rev. Fluids* **3**, 044303 (2018).
- [37] S. Chandrasekhar, *Hydrodynamic and Hydromagnetic Stability* (Dover Publications, New York, 1981).
- [38] A. Wyner, J. Ziv, and A. Wyner, *IEEE Trans. Inf. Theory* **44**, 2045 (1998).
- [39] S. Martiniani, P. M. Chaikin, and D. Levine, *Phys. Rev. X* **9**, 011031 (2019).
- [40] S. Ro, B. Guo, A. Shih, T. V. Phan, R. H. Austin, D. Levine, P. M. Chaikin, and S. Martiniani, *Phys. Rev. Lett.* **129**, 220601 (2022).
- [41] $\theta(\mathbf{x}, t) = \tan^{-1}(\frac{p_y}{p_x})$.
- [42] V. L. Berezinskii, *Sov. J. Exp. Theor. Phys.* **34**, 610 (1972).
- [43] J. M. Kosterlitz and D. J. Thouless, *J. Phys. C: Solid State Phys.* **6**, 1181 (1973).
- [44] J. M. Kosterlitz, *J. Phys. C: Solid State Phys.* **7**, 1046 (1974).
- [45] P. M. Chaikin and T. C. Lubensky, *Principles of Condensed Matter Physics* (Cambridge University Press, Cambridge, England, 1995).
- [46] J. M. Kosterlitz, *Rev. Mod. Phys.* **89**, 040501 (2017).
- [47] A. W. C. Lau and T. C. Lubensky, *Phys. Rev. E* **80**, 011917 (2009).
- [48] A. J. Bray, *Adv. Phys.* **51**, 481 (2002).
- [49] U. Frisch and A. N. Kolmogorov, *Turbulence: The Legacy of A.N. Kolmogorov* (Cambridge University Press, Cambridge, England, 1995).
- [50] S. Chandrasekhar, *Liquid Crystals*, 2nd ed. (Cambridge University Press, Cambridge, England, 1992).